ACS OMEGA

http://pubs.acs.org/journal/acsodf

Article

Increased Active Sites on Irregular Morphological α-Fe_2O_3 Nanorods for Enhanced Photoelectrochemical Performance

Jiawei Sun, Weiwei Xia,* Qian Zheng, Xianghua Zeng,* Wei Liu, Gang Liu, and Pengdi Wang

Cite This: *ACS Omega* 2020, 5, 12339−12345

Read Online

ACCESS | Metrics & More | Article Recommendations | Supporting Information

ABSTRACT: Uniform rectangular α-Fe_2O_3 nanorods (R-Fe_2O_3) and irregular α-Fe_2O_3 nanorods (D-Fe_2O_3) with a random size vertically aligned on fluorine-doped tin oxide were prepared with a facile one-step hydrothermal procedure. X-ray diffraction (XRD) measurements and Raman spectra confirm that the obtained samples are α-Fe_2O_3, and XRD patterns show that D-Fe_2O_3 has two extra (012) and (104) planes of hematite in addition to the identical peaks to R-Fe_2O_3. The carrier density of the D-Fe_2O_3 sample is four times larger than that of R-Fe_2O_3. Finally, the D-Fe_2O_3 photoelectrode exhibited a better photoelectrochemical (PEC) performance under visible illumination than that of R-Fe_2O_3, achieving the photocurrent density of 0.15 mA cm^{-2} at 1.23 V *versus* reversible hydrogen electrode. In addition, incident photo-to-current conversion efficiency of D-Fe_2O_3 is nearly three times larger than that of R-Fe_2O_3. Hence, the improved PEC performance of D-Fe_2O_3 can be ascribed to higher carrier density resulting from the amount of oxygen vacancies and more activated exposed surface facets.

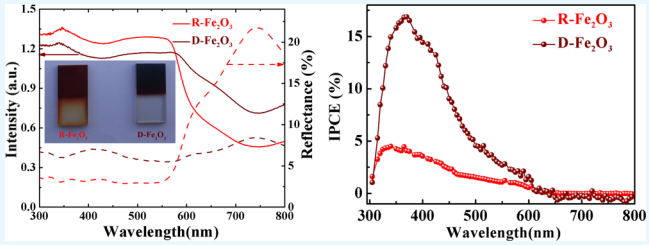

INTRODUCTION

Sunlight-driven photoelectrochemical (PEC) water splitting is one of the most promising strategies for the conversion of sunlight into hydrogen as a clean and renewable source of energy.[1−5] An efficient PEC process is rooted in appropriate semiconductor materials, which should possess a small band gap to ensure wide light harvest, facile charge separation to allow the generated photocharges to migrate to the reactive sites, and highly catalytic capability to fully utilize the separated photocharges.[6,7] Consequently, much effort and attention have been paid to explore all kinds of semiconductor materials as candidates for photoelectrodes. Among them, hematite (α-Fe_2O_3) is one promising candidate for photoanodes because of favorable combination merits of nontoxicity, vast abundance, small band gap (∼2.1 eV), favorable band edge positions, and good stability in aqueous solution.[8−10] α-Fe_2O_3 photoanodes could achieve a maximum theoretical solar-to-hydrogen efficiency of ∼16.8%.[11] Despite intensive efforts, the best reported efficiency can only reach 0.6%, which is too low to be compared to the theoretical predicted efficiency.[12] Pure α-Fe_2O_3 is severely restricted by some inherent drawbacks such as a very short hole diffusion length (∼2−4 nm) and poor majority carrier conductivity, which make it less competitive as compared with other material candidates. To address these limitations and obtain high-performance α-Fe_2O_3 photoanodes, a number of approaches have been explored to address these limitations such as element doping,[13−15] heterojunction formation,[16,17] morphology control,[18,19] and so forth. Among them, morphology control of photoanodes has shown promising PEC performance and received extensive research efforts.

α-Fe_2O_3 nanostructured arrays can improve the charge-carrier collection of photoanodes through minimizing hopping transport in the right direction toward the current collector and thus reducing recombination losses at the grain boundary.[20] FeOOH nanostructured arrays grown on conductive substrates are generally utilized as precursors for the fabrication of three-dimensional (3-D) α-Fe_2O_3 array photoelectrodes through a dehydration process with the thermal annealing process. According to the existing literature reports, in order to obtain α-Fe_2O_3 with excellent conductivity, it is necessary to increase the synthesis temperature to more than 800 °C.[21] However, such high thermal annealing times will result in the morphological change and impact the light absorption capability and the charge transport pathway toward the current collector of the α-Fe_2O_3 nanostructured photoelectrodes. To overcome the high-temperature annealing treatment, doping foreign ions or synthesizing novel nanostructures was used to enhance charge separation and transfer[22] because this novel strategy can provide high concentration of oxygen vacancies in α-Fe_2O_3 and improve

Received: March 10, 2020
Accepted: May 4, 2020
Published: May 18, 2020

https://dx.doi.org/10.1021/acsomega.0c01072
ACS Omega 2020, 5, 12339−12345

the electrical conductivity in essence. Besides, they can also increase the specific surface area on PEC properties.[23−27]

Another important aspect of developing an efficient hematite photoelectrode largely overlooked so far is to prepare Fe_2O_3 nanostructured materials with defined surface facets. Chen *et al.*[28] showed that the α-Fe_2O_3 exposed by {012} and {104} facets can facilitate the reduction of IO_3^-, which results in increasing the activity of photocatalytic water oxidation significantly. Lin *et al.*[29] showed the catalytic activity of hematite surface facets following the order of {113} > {104} > {001}. In addition, α-Fe_2O_3 nanosheets with exposed {104} facets were observed to be enhanced through hydrogenation.[30] However, the correlation mechanism of the exposed surface facets and the catalytic performance of α-Fe_2O_3 nanostructured materials are not fully understood.

Inspired by the abovementioned considerations, if the α-Fe_2O_3 photoelectrode can readily be fabricated with significant oxygen vacancies and have more activated exposed surface facets, the correspondingly enhanced conductivity and catalytic activity area would then contribute to the PEC performance. Herein, we have prepared uniform rectangular α-Fe_2O_3 nanorods (R-Fe_2O_3) and irregular α-Fe_2O_3 nanorods (D-Fe_2O_3) with a random size vertically aligned on fluorine-doped tin oxide (FTO) with a facile one-step hydrothermal procedure, where the D-Fe_2O_3 sample has more exposed {012} and {104} surface facets. Also, the D-Fe_2O_3 photoanode has a photocurrent density of 0.15 mA cm^{-2} at 1.23 V *versus* reversible hydrogen electrode (RHE) and an incident photo-to-current conversion efficiency (IPCE) of 17% can be achieved at 366 nm. Our studies will be helpful to the design of more effective PEC systems.

RESULTS AND DISCUSSION

The R-Fe_2O_3 and D-Fe_2O_3 nanostructured arrays were grown on FTO substrates using a facial hydrothermal and postannealing process. Schematic illustration of R-Fe_2O_3 and D-Fe_2O_3 arrays grown on the FTO substrate is illustrated in Figure 1a. The structures of R-Fe_2O_3 and D-Fe_2O_3 nanorod arrays were characterized by X-ray diffraction (XRD), and the results are presented in Figure 1b. The peaks are identical to the hexagonal structure (JCPDS 33-0664) of hematite polymorphs without impurity peaks except for the FTO substrate. XRD measurements showed that the major diffraction peaks of R-Fe_2O_3 and D-Fe_2O_3 arrays are almost the same, except for two additional peaks at 24.14 and 33.15° for D-Fe_2O_3, which correspond to (012) and (104) planes of hematite. According to the previous literature, (012) and (104) facets have higher catalytic activity compared to the common (101) and (111) planes.[30] Because of similar patterns among β-Fe_2O_3, γ-Fe_2O_3, and Fe_3O_4, the XRD patterns cannot provide enough evidence to confirm that the obtained nanorod arrays are α-Fe_2O_3. Raman spectroscopy measurements were performed using an excitation wavelength of 532 nm. There are four peaks centered at 225, 229, 412, and 1314 cm^{-1} for both R-Fe_2O_3 and D-Fe_2O_3, which confirmed the α-Fe_2O_3 structure shown in Figure S1 in the Supporting Information. The morphologies of the R-Fe_2O_3 and D-Fe_2O_3 nanostructured arrays were also investigated with scanning electron microscopy (SEM) images. Figure 1c,d shows the SEM images of the Fe_2O_3 nanorod arrays grown on the FTO substrates. The SEM images show that the R-Fe_2O_3 sample (Figure 1c) is composed with a lot of oriented and bundled rectangular nanorods with a diameter of ∼100 nm on the FTO substrate, while D-Fe_2O_3 is composed with irregular nanorods with a random size vertically aligned on the FTO substrate, that is, the nanorods have any shape or size, as shown in Figure 1d.

We further carried out transmission electron microscopy (TEM) and high-resolution TEM (HRTEM) characterization to investigate the inner crystal structures and microstructure features. The TEM image of a selected individual R-Fe_2O_3 nanorod is displayed in Figure 2a. The nanorod has a diameter of ∼200 nm, which is consistent with the result of the SEM image shown in Figure 1c. Furthermore, the HRTEM image (Figure S2 in the Supporting Information) shows that the *d*-spacing of 2.70 Å can be indexed to the (104) plane of the α-Fe_2O_3 phase. In contrast, different magnitudes of the diameter

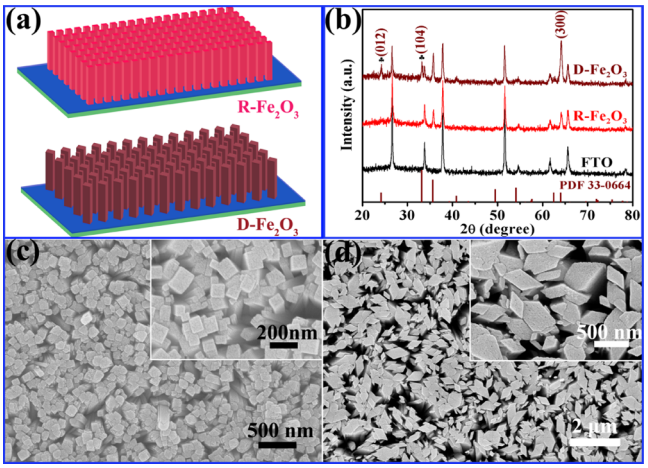

Figure 1. (a) Schematic illustration of R-Fe_2O_3 and D-Fe_2O_3 grown on the FTO substrate; (b) XRD patterns of R-Fe_2O_3 and D-Fe_2O_3 nanostructured arrays. (c,d) SEM images of R-Fe_2O_3 and D-Fe_2O_3 nanostructured arrays, respectively.

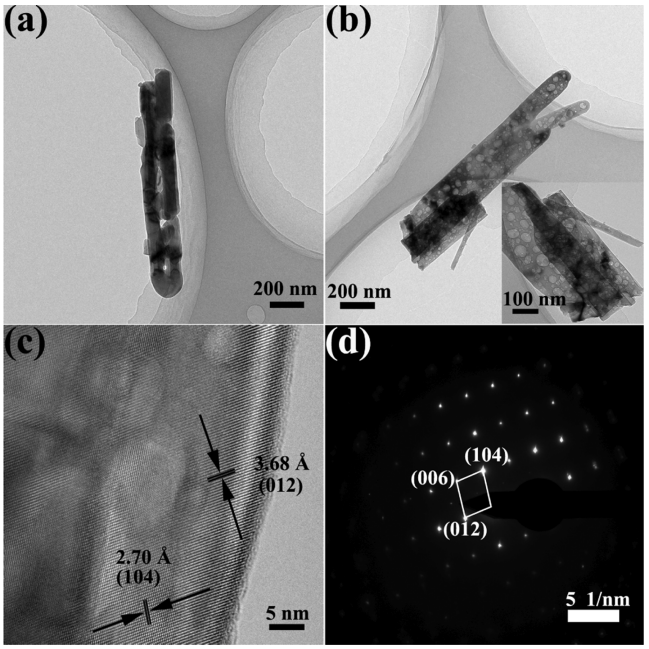

Figure 2. (a,b) Low-magnification images of an individual R-Fe_2O_3 and D-Fe_2O_3 nanorod. (c) High-magnification bright-field image of the D-Fe_2O_3 nanorod. (d) SAED pattern corresponding to the external side of the nanorod marked in (c).

https://dx.doi.org/10.1021/acsomega.0c01072
ACS Omega 2020, 5, 12339−12345

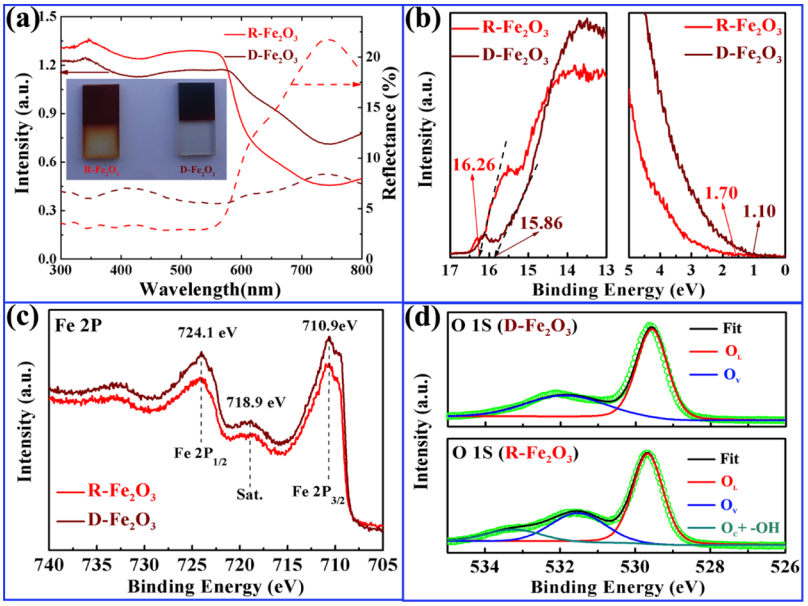

Figure 3. (a) Diffuse reflectance spectra measured with an integrating sphere and absorption spectra taken with reflectance and transmission (inset: a photograph of the R-Fe_2O_3 and D-Fe_2O_3 nanorod arrays on the FTO substrates after the postannealing process). (b) Ultraviolet photoelectron spectroscopy (UPS) secondary-electron cutoff and the VBM region. X-ray photoelectron spectroscopy (XPS) spectra of Fe 2p (c) and O 1s (d) for R-Fe_2O_3 and D-Fe_2O_3.

for D-Fe_2O_3 can be found; furthermore, there are many voids in the nanorods, as displayed in Figure 2b. The existence of the mesoporous nanostructure allows for electrolyte penetration and easy contact with the photoelectrode materials, which will be beneficial to shorten the hole transport distance from the photoelectrode to the electrode/electrolyte interface during the electrochemical measurement process. The HRTEM image (Figure 2c) also shows well-resolved lattice fringes with separations of 2.70 and 3.68 Å which match well with the interplanar spacing of (104) and (012), respectively. The HRTEM and SAED analyses confirm that the D-Fe_2O_3 nanorods are mainly enclosed by (104) and (012) facets, which is consistent with XRD analysis shown in Figure 1b. Clear SAED fringe patterns shown in Figure 2d are in harmony with the planes observed in the HRTEM image shown in Figure 2c.

The optical absorption, reflectance properties, and electronic nature of the band gap in hematite photoanodes are important to understand their PEC performance. In order to systematically understand the intrinsic optical properties of two samples, the light absorption and reflectance properties were measured and compared over a wavelength range from 300 to 800 nm. Figure 3a shows the diffuse reflectance and absorption spectra of R-Fe_2O_3 and D-Fe_2O_3. In the ultraviolet and visible region (wavelength range of 300−575 nm), R-Fe_2O_3 has a relatively high absorption and less reflectance percentage in comparison with D-Fe_2O_3 from 300 to 600 nm, implying that the ultraviolet and visible light can be effectively absorbed for the R-Fe_2O_3 photoanode. The direct band gap of hematite can be evaluated from extrapolating the linear portion of the Tauc relation ($(\alpha h\nu)^2$ *vs* $h\nu$), whose values are equal to 2.02 and 1.70 eV for R-Fe_2O_3 and D-Fe_2O_3, respectively (as shown in Figure S3). Interestingly, the D-Fe_2O_3 film photoanode exhibits the enhancement in near-infrared light absorption, which has potential application in a near-infrared photoelectric conversion device. The inset of Figure 3a depicts the digital photographs of R-Fe_2O_3 and D-Fe_2O_3 photoanodes for comparison. It is noted that D-Fe_2O_3 photoanodes are much darker as compared to R-Fe_2O_3 photoanodes, suggesting significantly enhanced red to near-infrared light owing to their unique morphological nanorod alternative arrangement.[31]

UPS measurements were carried out to check the difference of the surface electron behavior between R-Fe_2O_3 and D-Fe_2O_3, as shown in Figure 3b. The work function (ϕ) can be obtained by observing the low-energy secondary-electron cutoff, which is equal to 4.96 eV for the sample of R-Fe_2O_3 and 5.36 eV for the sample of D-Fe_2O_3. The valence band maximum (VBM) can be extracted from the spectra in UPS data, which is about 1.70 eV for R-Fe_2O_3 and 1.10 eV for D-Fe_2O_3. Combined with the energy band gaps, the conduction band and valence band (*vs* vacuum) of R-Fe_2O_3 and D-Fe_2O_3 can be obtained, as shown in Table 1. XPS is an effective

Table 1. Energy Level of R-Fe_2O_3 and D-Fe_2O_3

samples	E_g (eV)	E_C (eV *vs* Vac.)	E_F (eV *vs* Vac.)	E_V (eV *vs* Vac.)
R-Fe_2O_3	2.02	4.66	4.96	6.66
D-Fe_2O_3	1.70	4.76	5.36	6.46

method for analyzing the surface chemical state and the concentration of the hydroxyl group in native metal oxide nanomaterials. The introduction of oxygen vacancies or hydroxyl groups in obtained Fe_2O_3 samples will result in the change in electronic structure. Here, XPS spectra of Fe 2p and O 1s are shown in Figure 3c,d. Figure 3c shows the high-resolution Fe 2p emission spectra of R-Fe_2O_3 and D-Fe_2O_3 samples. The Fe $2p_{3/2}$ and Fe $2p_{1/2}$ peaks are located at the binding energies of 710.9 and 724.1 eV with a satellite peak at 718.9 eV, which are consistent with typical values for Fe^{3+} in Fe_2O_3. Figure 3d shows the high-resolution O 1s spectra of R-Fe_2O_3 and D-Fe_2O_3. It shows that each O 1s spectrum can be resolved into two or three Gaussian components. The lowest binding energy about 529.6 eV corresponds to the lattice oxygen O^{2-} (denoted as O_L). The middle binding energy

https://dx.doi.org/10.1021/acsomega.0c01072
ACS Omega 2020, 5, 12339−12345

located at ~531.5 eV corresponds to oxygen ions around the oxygen vacancy (denoted as O_V). The highest binding energy 533.2 eV belongs to the surface chemisorbed oxygen and −OH (denoted as O_C and −OH).[32] The relative percentages of O_L, O_V, O_C, and −OH components of R-Fe_2O_3 and D-Fe_2O_3 are estimated and summarized in Table 2. One can easily find that the D-Fe_2O_3 sample has a higher O_V, which will greatly influence PEC performance, as O_V plays the role of the inherent donors in the structure.[33]

Table 2. Relative Percentages of the O_L, O_V, O_C, and −OH Components for R-Fe_2O_3 and D-Fe_2O_3

sample		O_L	O_V	O_C & −OH
R-Fe_2O_3	binding energy (eV)	529.6	531.5	533.2
	relative percentage (%)	58.1%	29.9%	12%
D-Fe_2O_3	binding energy (eV)	529.6	531.8	
	relative percentage (%)	63.8%	36.2%	

To understand the charge transfer process occurring at the interface of the photoelectrode/electrolyte, electrochemical impedance spectroscopy (EIS) was carried out and the results are presented in Figure 4a. For each EIS spectrum, two distinct parts comprising a semicircle in the high-frequency region (in Figure S3b) and a straight slope in the low-frequency region are considered to be related to the charge transfer process and diffusion-limited process, respectively. The equivalent RC circuit was fitted to interpret the EIS results (see inset of Figure 4a). $R_{solution}$ is the solution resistance in series of the parallel RC that models the FTO/α-Fe_2O_3 interface ($R_{FTO/bulk}$ and $C_{FTO/bulk}$) at high frequencies, a resistance related to the rate of trapping holes (R_{bulk}), and a capacitance of the bulk hematite (C_{bulk}), the latter incorporated into the equivalent circuit by a constant phase element (CPE_{bulk}), the charge transfer resistance (R_{ct}), and a capacitance ($C_{interface}$) of the surface state relative to the electrode/electrolyte interface. It can be shown from the calculation results of an equivalent circuit that the charge transfer resistance (R_{ct}) of D-Fe_2O_3 is considerably lower than that of R-Fe_2O_3, which indicates that the resistance of the D-Fe_2O_3 electrode shows an ideal performance as it is smaller in comparison with the R-Fe_2O_3 electrode. Mott−Schottky plots of R-Fe_2O_3 and D-Fe_2O_3 electrodes were used to estimate the electron density (Figure 4b) using the following equation[34]

$$N_d = (2/e_0\varepsilon\varepsilon_0 A^2)[d(1/C^2)/dV]^{-1} \quad (1)$$

Here e_0, ε, and ε_0 are the electron charge with a value of 1.6×10^{19} C, dielectric constant with a value of 80,[35] and permittivity of vacuum with a value of 8.85×10^{-12} F·m^{-1}, respectively. A, N_d, V, and C are the area of the film electrode, the charge carrier density, the bias applied on the electrode, and the surface capacitance, respectively. Thus, N_d values of R-Fe_2O_3 and D-Fe_2O_3 electrodes are estimated to be 0.67×10^{18} and 2.8×10^{18} cm^{-3}, respectively. Thus, it is reasonable to conclude that the enhancement of the carrier density is due to the increment of the O_V component in the D-Fe_2O_3 electrode. Besides, the flat-band potentials derived from the Mott−Schottky plot are equal to 0.15 and 0.20 V *versus* RHE at pH 13.6 for R-Fe_2O_3 and D-Fe_2O_3 electrodes, respectively. The related conduction band *versus* RHE is equal to 0.15 and 0.20 V, which is consistent with the UPS measurements. From the abovementioned discussion, the conduction band and valence band (*vs* vacuum) and the energy band alignments of R-Fe_2O_3 and D-Fe_2O_3 are displayed in Figure 4c. Likewise, cyclic voltammetry (CV) of R-Fe_2O_3 and D-Fe_2O_3 and the difference in current density variation plotted against the scan rate are shown in Figure S4. The double-layer capacitance (C_{dl}) values of 0.91 and 0.97 mF/cm^2 are calculated for R-Fe_2O_3 and D-Fe_2O_3, respectively, indicating that D-Fe_2O_3 has more electrochemical active sites for the PEC process than R-Fe_2O_3. Figure 4d shows the current density *versus* applied potential under dark and light (simulated sunlight) conditions. D-Fe_2O_3 photoelectrodes presented the better PEC property under illumination than R-Fe_2O_3, achieving the photocurrent density of 0.15 mA cm^{-2} at 1.23 V *versus* RHE. The dark current can be ignored in comparison with the light one, meaning that e−p separation is dominated in the PEC process.

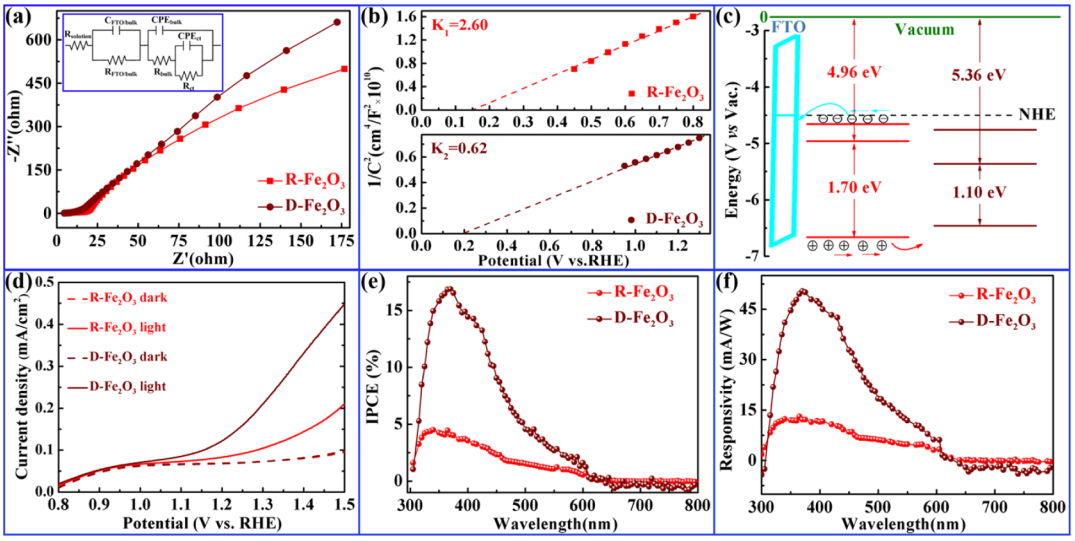

Figure 4. (a) EIS Nyquist plots of R-Fe_2O_3 and D-Fe_2O_3 photoanodes under dark conditions obtained in a frequency range from 1 to 500,000 Hz. (b) Mott−Schottky plot at 10 kHz of the PEC system with R-Fe_2O_3 and D-Fe_2O_3 photoanodes. (c) Proposed energy band alignment of R-Fe_2O_3 and D-Fe_2O_3 photoanodes. (d) Current density *vs* applied potential (J−V) curves. Changes of IPCE (e) and responsivity (f) with the wavelength.

https://dx.doi.org/10.1021/acsomega.0c01072
ACS Omega 2020, 5, 12339−12345

The IPCE spectra under zero bias voltage of R-Fe_2O_3 and D-Fe_2O_3 optoelectronic devices were obtained, as shown in Figure 4e. The IPCE value of D-Fe_2O_3 significantly enhanced compared with that of R-Fe_2O_3 with a wavelength from 300 to 600 nm. In addition, the maximum IPCE value of 17% was observed for D-Fe_2O_3 at 366 nm, which is approximately 3.7 times higher than that of R-Fe_2O_3. The value is superior to those in most other existing reports.[36−38] Moreover, the IPCE for R-Fe_2O_3 and D-Fe_2O_3 was especially low in the long-wavelength range (in the 600−800 nm region), which is consistent with the band gap of hematite. The wavelength-dependent responsivity $R(\lambda)$ can be calculated from the IPCE value using the following equation

$$R(\lambda) = \mathrm{IPCE} \times \frac{e\lambda}{hc} \quad (2)$$

where h is Planck's constant, c is the light speed in vacuum, and e is the elementary charge. The wavelength-dependent responsivity has a similar trend with that of the IPCE value. In addition, we also compare the PEC performance of α-Fe_2O_3 with other researchers' work (Table S1). The excellent responsivity performance of D-Fe_2O_3 might result from the amount of oxygen vacancies and more activated exposed surface facets.

CONCLUSIONS

To improve conductivity and to obtain more activated exposed surface facets, irregular Fe_2O_3 nanorods (D-Fe_2O_3) with a random size vertically aligned on FTO were prepared with a modulated hydrothermal procedure. The typical D-Fe_2O_3 exhibits a higher carrier density of 2.8×10^{18} cm^{-3} because of its higher oxygen vacancies. D-Fe_2O_3 photoelectrodes in PEC exhibited a better PEC performance under visible illumination with a photocurrent density of 0.15 mA cm^{-2} at 1.23 V *versus* RHE. Furthermore, D-Fe_2O_3 has a maximum IPCE value of 17% at 366 nm, which is approximately 3.7 times higher than that of R-Fe_2O_3. The improved IPCE is superior to many reported results. The same variation trend of the wavelength-dependent responsivity was also observed for D-Fe_2O_3 either. Our studies indicate that it is a good method to improve optoelectric properties *via* the morphological modulation.

EXPERIMENTAL SECTION

Materials. All chemicals were of analytical grade and used without further purification. Iron(III) chloride hexahydrate ($FeCl_3 \cdot 6H_2O$), ammonium ferrous sulfate hexahydrate ($(NH_4)_2Fe(SO_4)_2$), sodium sulfate (Na_2SO_4), urea ($CO(NH_2)_2$), sodium acetate ($CH_3COONa \cdot 3H_2O$), acetone, ethanol, and hydrochloric acid (HCl, 36.5−38% by weight) were purchased from Sinopharm Chemical Reagent Co., Ltd. Fluorine-doped tin oxide (SnO_2/F) conducting glass (FTO) was provided by Hefei Kejing Material Technology Co., Ltd.

Preparation of a Rectangular Bunched Fe_2O_3 (R-Fe_2O_3) Nanorod Array. The FTO glass substrate (1 × 2 cm) was cleaned with acetone, ethanol, and subsequently rinsed with deionized (DI) water and then was placed with the conducting side facing down in a Teflon-lined autoclave. FeOOH nanorods were grown in 20 mL of aqueous solution containing 0.15 M $FeCl_3$, 0.3 M urea, and 20 μL of HCl at 100 °C for 7 h. The prepared FeOOH samples were thoroughly washed with DI water to remove the salty residue, subsequently annealed at 550 °C under nitrogen flow for 2 h, and the R-Fe_2O_3 nanorods grown on the FTO substrate were obtained.

Synthesis of a Diamond Staggered Fe_2O_3 (D-Fe_2O_3) Nanorod Array. The precursor films of FeOOH nanorod arrays obtained by a modified hydrothermal method, which were grown on a cleaned FTO glass substrate (1 × 2 cm) in 20 mL of aqueous solution containing 0.2 M CH_3COONa, 0.1 M Na_2SO_4, and 0.1 M $(NH_4)_2Fe(SO_4)_2 \cdot 6H_2O$ at 100 °C for 7 h and then annealed at 550 °C under nitrogen flow for 2 h to prepare D-Fe_2O_3 nanorods on the FTO substrate.

Characterization. The crystal structure of the α-Fe_2O_3 nanorods was investigated by powder XRD (Bruker D8 ADVANCE) using Cu Kα (λ = 1.5406 Å) radiation. The morphology information of 3-D α-Fe_2O_3 arrays on the FTO substrate was acquired by field emission SEM (S-4800, Hitachi). HRTEM images were acquired from a Tecnai G2 F30 microscope. UV−visible spectra were recorded on a Varian Cary 5000 UV−visible spectrophotometer, and diffuse reflectance spectra and transmittance spectra were equipped with an integrating sphere. Raman measurements were performed at room temperature on a Renishaw inVia Reflex Raman spectrometer with 532 nm lines. XPS and UPS measurements were conducted on an ESCALAB-250Xi photoelectron spectroscope.

PEC Measurements. The electrochemical characteristics of the as-synthesized 3-D Fe_2O_3 photoanodes were evaluated by the curves of photocurrent density, CV, the current−voltage (J−V) characteristic of the electrodes, with a scan rate of 10 mV/s, EIS, and Mott−Schottky plots on the Zahner CIMPS electrochemical workstation (Germany) using a three-electrode cell. In addition, IPCE measurement was studied in a quartz cell, in which the 3-D Fe_2O_3 photoanode, a Pt wire, and an Hg/HgO were applied as the working, counter, and reference electrode, respectively. A 300 W Xe lamp (CEL-HXF 300, Beijing Au-light, China) was employed as an incident light source to study the PEC response of the samples. KOH (1 M) (pH = 13.6) solution was used as the electrolyte in this work.

ASSOCIATED CONTENT

Supporting Information

The Supporting Information is available free of charge at https://pubs.acs.org/doi/10.1021/acsomega.0c01072.

Raman spectra for R-Fe_2O_3 and D-Fe_2O_3 nanostructured arrays, high-magnification image of a selected individual R-Fe_2O_3 nanorod, band gaps for R-Fe_2O_3 and D-Fe_2O_3 samples, EIS spectra, LSV measurements, and comparison of PEC performance, and morphology of different hematites (PDF)

AUTHOR INFORMATION

Corresponding Authors

Weiwei Xia − *College of Physics Science and Technology & Institute of Optoelectronic Technology, Yangzhou University, Yangzhou 225002, P. R. China*; Email: wwxia@yzu.edu.cn

Xianghua Zeng − *College of Physics Science and Technology & Institute of Optoelectronic Technology and College of Electrical, Energy and Power Engineering, Yangzhou University, Yangzhou 225002, P. R. China*; orcid.org/0000-0003-4775-6764; Email: xhzeng@yzu.edu.cn

https://dx.doi.org/10.1021/acsomega.0c01072
ACS Omega 2020, 5, 12339−12345

Authors

Jiawei Sun − *College of Physics Science and Technology & Institute of Optoelectronic Technology, Yangzhou University, Yangzhou 225002, P. R. China*

Qian Zheng − *College of Physics Science and Technology & Institute of Optoelectronic Technology, Yangzhou University, Yangzhou 225002, P. R. China*

Wei Liu − *State Key Laboratory of Bioelectronics, School of Biological Sciences & Medical Engineering, Southeast University, Nanjing 210096, P. R. China*

Gang Liu − *College of Physics Science and Technology & Institute of Optoelectronic Technology, Yangzhou University, Yangzhou 225002, P. R. China*

Pengdi Wang − *College of Physics Science and Technology & Institute of Optoelectronic Technology, Yangzhou University, Yangzhou 225002, P. R. China*

Complete contact information is available at: https://pubs.acs.org/10.1021/acsomega.0c01072

Notes

The authors declare no competing financial interest.

■ ACKNOWLEDGMENTS

This work was supported by the National Key Research and Development Program of China (grant no. 2017YFB0403101) and the National Natural Science Foundation of China (grant 61604127 and 61474096).

■ REFERENCES

(1) Liu, J.; Zou, Y.; Jin, B.; Zhang, K.; Park, J. H. Hydrogen Peroxide Production from Solar Water Oxidation. *ACS Energy Lett.* **2019**, *4*, 3018−3027.

(2) Lumley, M. A.; Radmilovic, A.; Jang, Y. J.; Lindberg, A. E.; Choi, K.-S. Perspectives on the Development of Oxide-Based Photocathodes for Solar Fuel Production. *J. Am. Chem. Soc.* **2019**, *141*, 18358−18369.

(3) Takanabe, K. Photocatalytic Water Splitting: Quantitative Approaches toward Photocatalyst by Design. *ACS Catal.* **2017**, *7*, 8006−8022.

(4) Seo, J.; Nishiyama, H.; Yamada, T.; Domen, K. Visible-Light-Responsive Photoanodes for Highly Active, Stable Water Oxidation. *Angew. Chem., Int. Ed.* **2018**, *57*, 8396−8415.

(5) Yang, Y.; Niu, S.; Han, D.; Liu, T.; Wang, G.; Li, Y. Progress in Developing Metal Oxide Nanomaterials for Photoelectrochemical Water Splitting. *Adv. Energy Mater.* **2017**, *7*, 1700555.

(6) Nellist, M. R.; Mills, T. J.; Boettcher, S. W. Semiconductor-Electrocatalyst Interfaces: Theory, Experiment, and Applications in Photoelectrochemical Water Splitting. *Acc. Chem. Res.* **2016**, *49*, 733−740.

(7) Li, J.; Wu, N. Semiconductor-based photocatalysts and photoelectrochemical cells for solar fuel generation: a review. *Catal. Sci. Technol.* **2015**, *5*, 1360−1384.

(8) Shen, S.; Lindley, S. A.; Chen, X.; Zhang, J. Z. Hematite heterostructures for photoelectrochemical water splitting: rational materials design and charge carrier dynamics. *Energy Environ. Sci.* **2016**, *9*, 2744−2775.

(9) Chen, H. M.; Chen, C. K.; Liu, R.-S.; Zhang, L.; Zhang, J.; Wilkinson, D. P. Nano-architecture and material designs for water splitting photoelectrodes. *Chem. Soc. Rev.* **2012**, *41*, 5654−5671.

(10) Wang, F.; Li, Q.; Xu, D. Recent Progress in Semiconductor-Based Nanocomposite Photocatalysts for Solar-to-Chemical Energy Conversion. *Adv. Energy Mater.* **2017**, *7*, 1700529.

(11) Wang, G.; Ling, Y.; Wheeler, D. A.; George, K. E. N.; Horsley, K.; Heske, C.; Zhang, J. Z.; Li, Y. Facile Synthesis of Highly Photoactive α-Fe2O3-based Films for Water Oxidation. *Nano Lett.* **2011**, *11*, 3503−3509.

(12) Kim, J. Y.; Magesh, G.; Youn, D. H.; Jang, J. W.; Kubota, J.; Domen, K.; Lee, J. S. Single-crystalline, Wormlike Hematite Photoanodes for Efficient Solar Water Splitting. *Sci. Rep.* **2013**, *3*, 2681.

(13) Luo, Z.; Li, C.; Liu, S.; Wang, T.; Gong, J. Gradient Doping of Phosphorus in Fe_2O_3 Nanoarray Photoanodes for Enhanced Charge Separation. *Chem. Sci.* **2017**, *8*, 91−100.

(14) Kumari, S.; Singh, A. P.; Sonal; Deva, D.; Shrivastav, R.; Dass, S.; Satsangi, V. R. Spray Pyrolytically Deposited Nanoporous Ti^{4+} Doped Hematite Thin Films for Efficient Photoelectrochemical Splitting of Water. *Int. J. Hydrogen Energy* **2010**, *35*, 3985−3990.

(15) Xia, W.; Sun, J.; Zeng, X.; Wang, P.; Luo, M.; Dong, J.; Yu, H. FeO-based Hierarchical Structures on FTO Substrates and their Photocurrent. *Omega* **2020**, *5*, 2205−2213.

(16) McDonald, K. J.; Choi, K.-S. Synthesis and Photoelectrochemical Properties of $Fe_2O_3/ZnFe_2O_4$ Composite Photoanodes for Use in Solar Water Oxidation. *Chem. Mater.* **2011**, *23*, 4863−4869.

(17) Annamalai, A.; Shinde, P. S.; Subramanian, A.; Kim, J. Y.; Kim, J. H.; Choi, S. H.; Lee, J. S.; Jang, J. S. Bifunctional TiO_2 Underlayer for α-Fe_2O_3 Nanorod Based Photoelectrochemical Cells: Enhanced Interface and Ti^{4+} Doping. *J. Mater. Chem. A* **2015**, *3*, 5007−5013.

(18) Deng, J.; Zhong, J.; Pu, A.; Zhang, D.; Li, M.; Sun, X.; Lee, S.-T. Ti-Doped Hematite Nanostructures for Solar Water Splitting with High Efficiency. *J. Appl. Phys.* **2012**, *112*, 084312.

(19) Wang, L.; Fei, T.; Lou, Z.; Zhang, T. Three-Dimensional Hierarchical Flowerlike α-Fe_2O_3 Nanostructures: Synthesis and Ethanol-Sensing Properties. *ACS Appl. Mater. Interfaces* **2011**, *3*, 4689−4694.

(20) Qin, D.-D.; Tao, C.-L.; In, S.-i.; Yang, Z.-Y.; Mallouk, T. E.; Bao, N.; Grimes, C. A. Facile Solvothermal Method for Fabricating Arrays of Vertically Oriented α-Fe_2O_3 Nanowires and Their Application in Photoelectrochemical Water Oxidation. *Energy Fuels* **2011**, *25*, 5257−5263.

(21) Liao, A.; He, H.; Tang, L.; Li, Y.; Zhang, J.; Chen, J.; Chen, L.; Zhang, C.; Zhou, Y.; Zou, Z. Quasi-Topotactic Transformation of FeOOH Nanorods to Robust Fe_2O_3 Porous Nanopillars Triggered with a Facile Rapid Dehydration Strategy for Efficient Photoelectrochemical Water Splitting. *ACS Appl. Mater. Interfaces* **2018**, *10*, 10141−10146.

(22) Wang, D.; Chen, H.; Chang, G.; Lin, X.; Zhang, Y.; Aldalbahi, A.; Peng, C.; Wang, J.; Fan, C. Uniform Doping of Titanium in Hematite Nanorods for Efficient Photoelectrochemical Water Splitting. *ACS Appl. Mater. Interfaces* **2015**, *7*, 14072−14078.

(23) Campbell, C. T.; Peden, C. H. F. CHEMISTRY: Oxygen Vacancies and Catalysis on Ceria Surfaces. *Science* **2005**, *309*, 713−714.

(24) Cheng, F.; Zhang, T.; Zhang, Y.; Du, J.; Han, X.; Chen, J. Enhancing Electrocatalytic Oxygen Reduction on MnO_2 with Vacancies. *Angew. Chem., Int. Ed.* **2013**, *52*, 2474−2477.

(25) Kong, M.; Li, Y.; Chen, X.; Tian, T.; Fang, P.; Zheng, F.; Zhao, X. Tuning the Relative Concentration Ratio of Bulk Defects to Surface Defects in TiO2 Nanocrystals Leads to High Photocatalytic Efficiency. *J. Am. Chem. Soc.* **2011**, *133*, 16414−16417.

(26) Zhao, H.; Wang, J.; Zhang, L.; Rong, Y.; Chen, J.; Ibrahim, K.; Xing, X. Effects of Oxygen Vacancy on the Electronic Structure and Multiferroics in Sol-gel Derived $Pb_{0.8}Co_{0.2}TiO_3$ Thin Films. *Dalton Trans.* **2013**, *42*, 10358−10364.

(27) Zhang, Z.; Karimata, I.; Nagashima, H.; Muto, S.; Ohara, K.; Sugimoto, K.; Tachikawa, T. Interfacial oxygen vacancies yielding long-lived holes in hematite mesocrystal-based photoanodes. *Nat. Commun.* **2019**, *10*, 4832.

(28) Wang, Y. L.; Li, Y. H.; Wang, X. L.; Hou, Y.; Chen, A. P.; Yang, H. G. Effects of redox mediators on α-Fe_2O_3 exposed by {012} and {104} facets for photocatalytic water oxidation. *Appl. Catal., B* **2017**, *206*, 216−220.

(29) Chan, J. Y. T.; Ang, S. Y.; Ye, E. Y.; Sullivan, M.; Zhang, J.; Lin, M. Heterogeneous photo-Fenton reaction on hematite (α-Fe_2O_3) {104}, {113} and {001} surface facets. *Phys. Chem. Chem. Phys.* **2015**, *17*, 25333−25341.

(30) Ren, Y.; Yang, J.; Ma, Y.; Liu, B.; Zhang, X.; Wang, L.; Yuan, Y.; Liu, J.; Wang, M.; Du, Q.; Zhao, H.; Yang, H. Increasing sensing sensitivity of the Fe-α-Fe_2O_3 (104) surface by hydrogenation and the sensing reaction molecule mechanism. *Sens. Actuators, B* **2019**, *281*, 366−374.
(31) Jung, J.-Y.; Guo, Z.; Jee, S.-W.; Um, H.-D.; Park, K.-T.; Hyun, M. S.; Yang, J. M.; Lee, J.-H. A waferscale Si wire solar cell using radial and bulk p-n junctions. *Nanotechnology* **2010**, *21*, 445303.
(32) Dou, Z. F.; Cao, C. Y.; Wang, Q.; Qu, J.; Yu, Y.; Song, W. G. Synthesis, self-assembly, and high performance in gas sensing of X-shaped iron oxide crystals. *ACS Appl. Mater. Interfaces* **2014**, *4*, 5698−5703.
(33) Baek, M.; Kim, D.; Yong, K. Simple but Effective Way To Enhance Photoelectrochemical Solar-Water-Splitting Performance of ZnO Nanorod Arrays: Charge-Trapping Zn(OH)2 Annihilation and Oxygen Vacancy Generation by Vacuum Annealing. *ACS Appl. Mater. Interfaces* **2017**, *9*, 2317−2325.
(34) Zhao, X.; Feng, J.; Chen, S.; Huang, Y.; Sum, T. C.; Chen, Z. New Insight into the Roles of Oxygen Vacancies in Hematite for Solar Water Splitting. *Phys. Chem. Chem. Phys.* **2017**, *19*, 1074−1082.
(35) Cesar, I.; Sivula, K.; Kay, A.; Zboril, R.; Grätzel, M. Influence of Feature Size, Film Thickness, and Silicon Doping on the Performance of Nanostructured Hematite Photoanodes for Solar Water Splitting. *J. Phys. Chem. C* **2008**, *113*, 772−782.
(36) Peeters, D.; Sadlo, A.; Lowjaga, K.; Mendoza Reyes, O.; Wang, L.; Mai, L.; Gebhard, M.; Rogalla, D.; Becker, H.-W.; Giner, I.; Grundmeier, G.; Mitoraj, D.; Grafen, M.; Ostendorf, A.; Beranek, R.; Devi, A. Nanostructured Fe_2O_3 Processing via Water-Assisted ALD and Low-Temperature CVD from a Versatile Iron Ketoiminate Precursor. *Adv. Mater. Interfaces* **2017**, *4*, 1700155.
(37) Wang, Z.; Zou, G.; Wang, W.; Tang, Z.; Bi, Y.; Wang, X. Melamine-assisted to fabricate pure α-Fe_2O_3 polyhedron with high index facet exposed as an effective photoelectrode. *J. Power Sources* **2017**, *343*, 94−102.
(38) Dias, P.; Andrade, L.; Mendes, A. Hematite-based photoelectrode for solar water splitting with very high photovoltage. *Nano Energy* **2017**, *38*, 218−231.

https://dx.doi.org/10.1021/acsomega.0c01072
ACS Omega 2020, 5, 12339−12345